




RESEARCH ARTICLE OPEN ACCESS

Titanium-Doped In_2O_3 : A High-Mobility, Thermally Stable Back Contact for Bifacial Chalcopyrite Solar Cells

Jan Keller¹  | Sapna Mudgal¹ | Ana Jurado-Estrada² | Mustafa Togay²  | Jake W. Bowers²  | Marika Edoff¹

¹Division of Solar Cell Technology, Ångström Laboratory, Uppsala University, Uppsala, Sweden | ²Centre for Renewable Energy Systems Technology (CREST), Wolfson School of Mechanical, Electrical and Manufacturing Engineering, Loughborough University, Loughborough, UK

Correspondence: Jan Keller (jan.keller@angstrom.uu.se)

Received: 15 December 2025 | **Revised:** 31 January 2026 | **Accepted:** 3 February 2026

Keywords: (Ag,Cu)(In,Ga)Se₂ | bifacial solar cell | CIGS | high-mobility transparent conductive oxide | In_2O_3 :Ti

ABSTRACT

This study evaluates In_2O_3 :Ti as a transparent back contact (TBC) material in bifacial (Ag,Cu)(In,Ga)Se₂ (ACIGS) solar cells with a band gap of 1.1 eV and compares it to commonly used In_2O_3 :Sn. Both TBC layers were processed with a sheet resistance $\leq 10 \Omega/\text{sq}$, as required in a monolithically series-connected ACIGS module. In contrast to several other high-mobility TBCs previously tested in ACIGS solar cells, In_2O_3 :Ti retains its exceptionally high mobility ($>100 \text{ cm}^2/\text{Vs}$), low resistivity ($2.4 \cdot 10^{-4} \Omega\text{cm}$), and minimal near-infrared absorption ($<5\%$ at ACIGS bandgap) after high-temperature absorber deposition. As a result, an up to $3 \text{ mA}/\text{cm}^2$ higher short-circuit current density is measured under rear illumination for cells with an In_2O_3 :Ti back contact as compared with devices using highly doped In_2O_3 :Sn. The best cell reaches an efficiency of 10.2% at rear illumination with a bifaciality factor of 68%. At front illumination, the cell performance is on the same level for both TBCs.

1 | Introduction

Solar cells based on the chalcopyrite absorber material (Ag, Cu)(In,Ga)Se₂ (ACIGS) have reached efficiencies (η) of up to 23.6% on opaque Mo back electrodes [1] and 19.8% in bifacial configuration, using In_2O_3 :Sn (ITO) as a transparent back contact (TBC) [2]. In the latter case, a bifaciality factor of 55% was achieved (i.e. $\eta = 10.9\%$ at rear illumination). To date, the performance at rear illumination is mainly limited by the lower short-circuit current density (J_{SC}), which can be explained by two factors:

(1) *Electrons generated close to the back contact have a relatively small chance to reach the n-type buffer layer at the front.* The low collection efficiency close to and at the TBC arises from the finite electron diffusion length in the ACIGS bulk, back contact recombination and the potentially excessive formation of GaO_x (leading to a reversal of the intended back-surface field [3, 4]), as well as the typically higher Ga content at the back (resulting in increased nonradiative recombination via defects [5–10]). Possible pathways to minimize collection losses at rear illumination include

narrowing the width of the high-Ga region at the back, for example by reducing the ACIGS deposition temperature, which also reduces GaO_x formation [2, 11], and extending the space-charge region width, for instance through sufficient Ag-alloying, which has previously been found to lead to lower net doping concentration [12–17].

(2) *Highly doped TBC materials absorb a large fraction of the incoming near-infrared (NIR) light.* Different n-type transparent conductive oxides (TCOs) were tested as a back contact for (A) CIGS solar cells, including SnO_2 :F (FTO) [18–25], ZnO:Al (AZO) [19, 22, 26–28], ZnO:B (BZO, unpublished in-house experiments), In_2O_3 :Sn (ITO) [2, 11, 19, 23, 25, 28–43], In_2O_3 :H (IOH) [3, 4, 44], In_2O_3 :W (IWO) [13, 14, 45], In_2O_3 :Zr (IZrO) [46], In_2O_3 :Zn (IZnO) [46], and In_2O_3 :Ti (ITiO) [47]. Except for FTO and BZO, all of these films were sputter-deposited. To minimize optical losses in the solar cell via free charge carrier absorption (FCA), those TBC films should exhibit the highest possible mobility (μ) and a sufficiently low free carrier concentration (N), such that the plasma wavelength (λ_p , i.e. peak in

This is an open access article under the terms of the [Creative Commons Attribution](https://creativecommons.org/licenses/by/4.0/) License, which permits use, distribution and reproduction in any medium, provided the original work is properly cited.

© 2026 The Author(s). *Solar RRL* published by Wiley-VCH GmbH.

FCA) is placed well outside the spectrally active region of the ACIGS absorber [48]. For standard ACIGS absorbers with a band gap (E_G) of 1.0–1.2 eV (i.e., absorption down to $\lambda \approx 1300$ nm), a value of $\lambda_p \geq 2 \mu\text{m}$ is deemed appropriate to avoid substantial optical losses via FCA in the TBC. Figure 1 summarizes the approximate ranges of the reported mobility and carrier concentration values for the abovementioned TCOs [49–54]. Here, only values for sputter-deposited films were considered, except for BZO and FTO, which are typically grown via chemical vapor deposition (CVD). For various film thicknesses (d_{TBC}), lines with a constant sheet resistance (R_{sheet}) of $10 \Omega/\text{sq}$ are added, determined by the corresponding μ - N couples and using the relationship:

$$\mu = \frac{1}{e \cdot N \cdot R_{\text{sheet}} \cdot d_{\text{TBC}}}$$

where e is the elementary charge. This specific R_{sheet} value is chosen, since $R_{\text{sheet}} \leq 10 \Omega/\text{sq}$ is needed for the electrodes in a full-scale, monolithically connected ACIGS module to avoid substantial fill factor (FF) losses [55, 56] and/or the need for metal grid fingers. The red lines highlight carrier concentrations corresponding to plasma wavelengths of 1–4 μm , assuming a high-frequency permittivity of $\epsilon_\infty = 4$ and an effective electron mass of $m^* = 0.30 m_e$ (m_e being the free electron mass), as calculated from [48]:

$$\lambda_p = 2\pi c \sqrt{\frac{\epsilon_0 \epsilon_\infty m^*}{N e^2}}$$

where ϵ_0 is the vacuum permittivity and c the speed of light. The ϵ_∞ and m^* numbers are average values reported in literature. In practice, they vary slightly between different TCO materials and

further depend on the exact film properties (e.g., crystallinity and doping level) [57–60].

As shown in Figure 1, the most commonly used TBC materials for thin-film solar cells, ITO and FTO, are often too highly doped to avoid a considerable amount of parasitic FCA ($N > 3.3 \cdot 10^{20} \text{ cm}^{-3}$ gives $\lambda_p < 2 \mu\text{m}$). This makes these two TCOs unsuitable as a back contact in bifacial ACIGS modules. Lower parasitic absorption can be achieved by using low-doped AZO or BZO instead. However, their mobility is typically limited to $\mu < 40 \text{ cm}^2/\text{Vs}$ (similar range as for ITO and FTO), leading to a quite low conductivity. Thus, AZO and BZO films would need to be >700 nm and $>2 \mu\text{m}$ thick to reach $R_{\text{sheet}} \leq 10 \Omega/\text{sq}$, respectively. Besides leading to higher material consumption, this may cause detrimental absorption of visible light for films being under-stoichiometric in oxygen and an increasing band-to-band absorption (losses in ultraviolet region). Furthermore, we found that CVD-BZO processed at temperatures $T < 200^\circ\text{C}$ severely decomposes during high-temperature ($T > 500^\circ\text{C}$) absorber growth (results not shown here).

Highest mobilities can be reached for hydrogen-doped In_2O_3 films (adding either H_2O or H_2), sometimes co-doped by metals like Ce or W [52]. These films can obtain $\mu > 150 \text{ cm}^2/\text{Vs}$ if they are first deposited in an amorphous state at room temperature ($\mu \approx 50 \text{ cm}^2/\text{Vs}$) and then post-annealed at $T \geq 150^\circ\text{C}$, activating a solid-phase crystallization (spc) [61]. Such TCOs would be perfect candidates for TBCs, since they reach a high conductivity at a doping level low enough to suppress substantial losses via FCA. Unfortunately, these films start to degrade when subjected to temperatures above $\approx 300^\circ\text{C}$, due to H_2O effusion from the layers [62, 63]. This very much limits the allowed thermal budget during ACIGS growth. Indeed, when IOH was used as a TBC for (A)CIGS solar cells processed at $T = 550^\circ\text{C}$, its sheet resistance increased up to fourfold [3, 4], making it unsuitable for bifacial ACIGS modules, too.

Lastly, sputter-deposited In_2O_3 films without hydrogen doping, but exclusively doped by transition metals (Me) like W, Ti, Zn, or Zr or by the lanthanide metal Ce can reach decent mobilities in the range of $\mu \approx 60$ – $110 \text{ cm}^2/\text{Vs}$, with carrier concentrations low enough ($N \approx 1.5$ – $3.5 \cdot 10^{20} \text{ cm}^{-3}$) to mitigate FCA losses in ACIGS solar cells [47, 52, 54]. These TCOs are typically grown directly crystalline at $T \geq 200^\circ\text{C}$, often followed by post-annealing at higher T to improve the mobility [62]. Most of those films showed no conductivity degradation (rather the opposite) for vacuum annealing temperatures up to at least 500°C [62, 63]. Theoretically, this makes In_2O_3 :Me films very suitable as a TBC in ACIGS solar cells and modules. However, most of the corresponding, hitherto tested TBCs showed either reduced transmission (IZrO) or reduced conductivity (IZnO) after high-temperature absorber growth [46]. Furthermore, our group evaluated IWO as a TBC for wide-gap ACIGS solar cells and also found an increase in R_{sheet} by a factor of 3–4 after ACIGS deposition [13, 14, 45], presumably resulting from a defective sputter target (substantially too low W content). The only report of a temperature-stable and highly NIR-transparent TBC for CIGS solar cells dates back to 2007, when Nakada et al. used ITiO ($R_{\text{sheet}} = 8 \Omega/\text{sq}$), reaching an efficiency of 11.3% at front and 8.9% at rear illumination [47]. The significant potential of Ti doping in sputtered In_2O_3 films had been identified and reported shortly beforehand [64, 65].

In our present work, we directly compare standard ITO to a high-mobility ITiO transparent back contact, both with

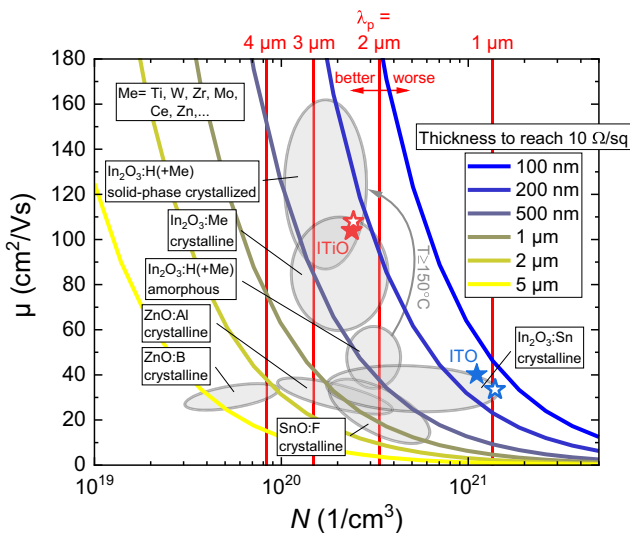


FIGURE 1 | Approximate ranges of reported mobility and carrier concentration values for the most common TCO materials prepared by sputtering (except for BZO and FTO, usually deposited via CVD) [49–54]. Lines of constant sheet resistance of $10 \Omega/\text{sq}$ (standard value in thin-film modules) are added for different film thicknesses. The red lines display the estimated carrier concentrations leading to plasma wavelengths of 1, 2, 3 and 4 μm (a value $\geq 2 \mu\text{m}$ is desirable for transparent back contacts in ACIGS solar cells). The stars represent the measured data of the ITO and ITiO samples from this study, before (filled) and after (open) absorber deposition.

module-compatible $R_{\text{sheet}} \leq 10 \Omega/\text{sq}$. A small amount of Ag ($[\text{Ag}]/([\text{Ag}] + [\text{Cu}]) = \text{AAC} = 0.1$) is added to the absorber to form high-quality ACIGS films at a deposition temperature as low as 450°C [2, 66–68]. The lower-than-standard deposition temperature mitigates GaO_x formation at the TBC/ACIGS interface and reduces a detrimental smear-out of the intended, steep Ga grading toward the back contact [2, 11].

2 | Results and Discussion

Two 3-stage co-evaporation runs were conducted to deposit ACIGS absorbers with a thickness of $d_{\text{abs}} \approx 1 \mu\text{m}$ and very similar composition of $\text{AAC} \approx 0.1$ and $\text{GGI} ([\text{Ga}]/([\text{Ga}] + [\text{In}])) \approx 0.2$, leading to a band gap of $E_G \approx 1.1 \text{ eV}$ (deduced from inflection point in external quantum efficiency (EQE) spectra). Run number 1 produced a rather off-stoichiometric absorber, with $([\text{Ag}] + [\text{Cu}])/([\text{In}] + [\text{Ga}]) = \text{I/III} \approx 0.8$, while the second run targeted a very close-stoichiometric ACIGS with $\text{I/III} \approx 1.0$. The exact in-depth average compositions, as determined by X-ray fluorescence (XRF) spectroscopy, are summarized in Table 1, together with

the corresponding best solar cell parameters, which will be discussed later.

The ITO films are 180 nm and the ITiO films 240 nm thick (more on TBC properties below). Since the Na diffusion from the soda-lime glass (SLG) substrates into the ACIGS films is insufficient when TBCs are used (in contrast to standard Mo) [4], a thin NaF precursor was deposited on top of the back contacts. The final devices have a CdS buffer and a ZnO:Al window layer.

In the following, the results are presented in three parts. First, the microstructure and compositional depth-profiles are illustrated. Then, the optical and electrical properties of the TBC films, before and after ACIGS deposition, are compared. Finally, in part three, the corresponding solar cell characteristics are shown and discussed.

2.1 | Chemical and Microstructural Analysis of the Solar Cells

Figure 2 shows the cross-sectional, scanning-electron microscopy (SEM) images of cells with ITO and ITiO back contacts from both absorber deposition runs. The images are representative for the

TABLE 1 | Absorber properties and corresponding JV -parameters of the best solar cells from the two ACIGS deposition runs conducted in this study. The JV -parameters are shown for front and rear illumination for samples with either ITO or ITiO back contacts. The $J_{SC,qe}$ values are calculated from the corresponding EQE spectra, assuming an AM1.5G illumination spectrum. These values are used to deduce the respective, corrected efficiencies $\eta_{qe} = \eta_{iv}(J_{SC,qe}/J_{SC,iv})$.

Run#	AAC	GGI	I/III	d_{abs} (μm)	E_G (eV)	TBC	Illum.	FF (%)	V_{OC} (mV)	$J_{SC,iv}$ (mA/cm^2)	$J_{SC,qe}$ (mA/cm^2)	η_{iv} (%)	η_{qe} (%)
1	0.12	0.20	~ 0.80	0.94	1.10	ITO	Front	76.1	577	30.2	31.9	13.3	14.0
							Rear	71.2	563	18.4	16.7	7.4	6.7
						ITiO	Front	75.0	564	31.1	30.9	13.1	13.1
							Rear	70.6	571	21.0	19.4	8.5	7.8
2	0.08	0.20	~ 1.00	1.06	1.11	ITO	Front	75.9	587	31.4	34.6	14.0	15.4
							Rear	76.0	588	19.6	19.7	8.8	8.8
						ITiO	Front	76.1	581	31.6	34.1	14.0	15.1
							Rear	75.4	595	23.4	22.7	10.5	10.2

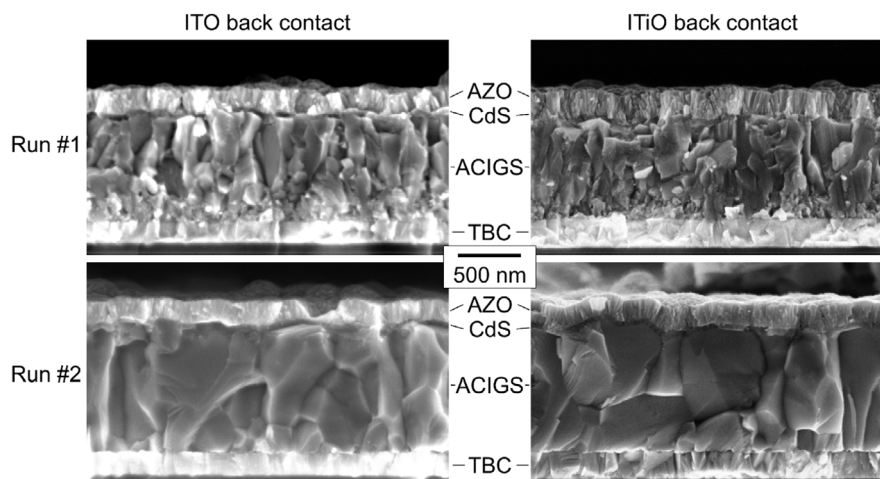


FIGURE 2 | Scanning-electron microscopy images of the cross-sections of cells with ITO (left) and ITiO (right) back contacts for samples from run number 1 (top, i.e., off-stoichiometric) and from run number 2 (bottom, i.e., close-stoichiometric). The scale bar is valid for all images.

entire sample areas, showing very similar ACIGS morphologies (i.e., grain size and roughness) for both TBCs. Although Ag was added, the absorber grain size is quite small for the off-stoichiometric sample from run number 1, showing the smallest grains close to the back contact, which often correlates with an increased Ga content [1, 69]. It may be assumed that these samples did not reach a group I-rich composition at all during growth (i.e., $I/III < 1$ at all times). The close-stoichiometric ACIGS films show significantly larger grains, due to the formation of I-rich phases during the second stage of the absorber deposition, facilitating grain growth. However, compared with highest-efficiency ACIGS devices [1], the grain size is still rather moderate, with grains rarely stretching from the front to the back electrode.

Figure 3 illustrates the quantified (from cross-calibration to XRF average compositions) AAC and GGI depth-profiles of all samples (without front TCO), as deduced from glow-discharge optical emission spectroscopy (GDOES). The normalized Cd signals and the onsets of the O signals are added as well, to highlight the depth of the CdS/ACIGS and ACIGS/TBC interfaces. A “notch” GGI profile is evident for both off-stoichiometric samples from run number 1, with the minimum value in the middle of the absorber, a slightly higher GGI close to the surface and a steep Ga increase toward the TBCs. The rather small extension of the high-Ga region at the back is deemed beneficial especially at rear illumination, shifting most of the carrier generation away from the TBC and minimizing recombination losses in its vicinity [2]. However, the increase in GGI toward the front surface may be detrimental at rear illumination, since it produces an electric field that opposes electron diffusion to the buffer, thereby reducing the collection efficiency in the bottom half of the absorber. In case of the close-stoichiometric samples from run number 2, the GGI is continuously increasing from the front to the back, with a significantly lower GGI at the interface to the TBC. The difference in Ga distribution between the first and second run suggests that the final GGI profile not only depends on the Ag content and deposition temperature, but also on the overall group-I supply and the formation of I-rich phases during growth.

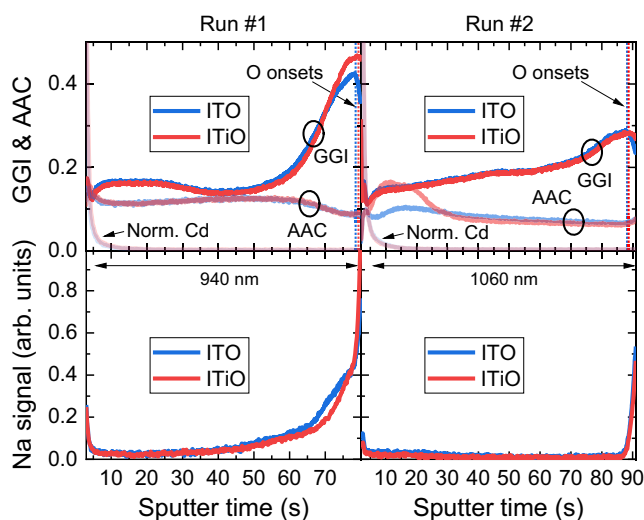


FIGURE 3 | (Top) Compositional (GGI and AAC) depth-profiles of the samples (no front TCO) with ITO and ITiO back contacts from both runs, as deduced from GDOES. The normalized Cd signals as well as the onsets of the O signals are added, too. (Bottom) Corresponding nonquantified Na profiles. For each individual run the same x-axes are used.

Substantial GaO_x formation typically results in a sharp GGI peak at the ACIGS/TBC interface in GDOES measurements, sometimes accompanied by a reversal of the GGI profile toward the TBC [3, 4, 44]. This is not observed in any of the samples, indicating that only a very moderate (if any) GaO_x layer formed at the rear interface. In a previous study, the same ACIGS deposition protocol was analyzed by energy-dispersive X-ray spectroscopy in transmission electron microscopy and we measured an approximately 3 nm-thick GaO_x layer with an ITO TBC [70]. A similar GaO_x extension is expected for the samples in this work. As a typical feature in ACIGS absorbers, the AAC profiles are anti-correlated to the GGI profiles, being a thermodynamically driven feature described in [71]. Due to space limitations, the GDOES analysis of the sample with ITiO from the second run had to be done at an outer, group-I rich position, explaining the higher AAC at the surface, presumably arising from the presence of Ag-rich phases.

The sodium distribution is not significantly affected by the choice of the TBC, as shown in the bottom part of Figure 3. In all cases, highest Na concentrations are found at the interfaces. The Na content in the ACIGS bulk is higher for the off-stoichiometric absorbers from run number 1, for which it increases toward the back contact. This feature can be explained by the higher density of grain boundaries (compare Figure 2), which are typically decorated by sodium [69, 72, 73].

Overall, no clear differences in absorber properties could be detected when comparing samples with ITO and ITiO back contacts. This is in line with earlier reports, suggesting that the back contact material does not significantly affect the absorber growth, as long as an excessive GaO_x formation can be avoided [4, 44]. The deposition temperature of 450°C applied in this work was obviously low enough to sufficiently mitigate GaO_x growth. In addition, no signs of Ti or Sn diffusion into the absorber were detected for ITiO and ITO TBCs, respectively (not shown here).

2.2 | Electrical and Optical Characterization of the Transparent Back Contacts

The aim of this work is to evaluate ITiO as a potentially temperature-stable TBC with a high NIR transparency at $R_{\text{sheet}} \leq 10 \Omega/\text{sq}$, required for module integration. As discussed in the introduction, the mobility and charge carrier density determine the optical properties of the TCOs. Thus, Hall-effect measurements were conducted on the ITO and ITiO films before and after ACIGS deposition. In the latter case, the absorber was mechanically removed with a scalpel. Table 2 summarizes the corresponding results. First of all, the R_{sheet} value of the ITO ($\approx 8 \Omega/\text{sq}$) is slightly lower as compared with the ITiO ($\approx 10 \Omega/\text{sq}$) layer. However, both films fulfill the requirement of $R_{\text{sheet}} \leq 10 \Omega/\text{sq}$. Also, none of the TBCs show any degradation in conductivity after high-temperature ACIGS processing, maintaining almost the exact same electrical parameters as measured in the respective initial states.

As intended, the ITiO film exhibits a significantly higher mobility of $\mu > 100 \text{ cm}^2/\text{Vs}$ and lower carrier density of $N = 2.4 \cdot 10^{20} \text{ cm}^{-3}$ than the ITO layer. The data points are added to Figure 1, being within the reported μ - N ranges of the corresponding material types. The measured N values should result in FCA maxima at $\lambda_p \approx 1.0$ – $1.1 \mu\text{m}$ and $\lambda_p \approx 2.3$ – $2.4 \mu\text{m}$ for ITO and ITiO,

TABLE 2 | Electrical properties of the ITO and ITiO back contact films before and after ACIGS deposition, as deduced from Hall-effect measurements.

TBC	Thickness (nm)	State	R_{sheet} (Ω/sq)	μ (cm^2/Vs)	N (cm^{-3})	ρ (Ωcm)
ITO	180	As grown	7.8	40.2	$1.1 \cdot 10^{21}$	$1.4 \cdot 10^{-4}$
		In device	7.4	33.5	$1.4 \cdot 10^{21}$	$1.3 \cdot 10^{-4}$
ITiO	240	As grown	10.5	104	$2.4 \cdot 10^{20}$	$2.5 \cdot 10^{-4}$
		In device	9.9	108	$2.4 \cdot 10^{20}$	$2.4 \cdot 10^{-4}$

respectively, using the same parameters for the calculation as above [48].

Figure 4 presents the absorptance (A) spectra of both TBC films, as derived from reflectance (R) and transmission measurements. A general observation is that the absorption of the TBC layers is not significantly affected by the ACIGS deposition process. The overall slightly higher A after absorber growth for ITO is likely caused by ACIGS residuals, which could not be completely removed via mechanical scratching (removal was smoother and more efficient for ITiO). It is suggested that due to the surface roughness of the remaining ACIGS layer, some of the light is refracted at high enough angles to be laterally out-coupled through the edges of the SLG during the optical measurement. This causes an “artificial” overestimation of the absorption. The presence of these residuals is further evident by the higher A in the visible spectral range (see A at $\lambda \approx 500$ nm for both films). Thus, it can be assumed that the absorption losses in the final solar cells are close to the A spectra of the as grown films. Both layers have a band gap of $E_G > 3.6$ eV, meaning that inter-band absorption losses can be neglected at rear illumination. Below the band gap energy, ITO and ITiO show a small absorption of $A \approx 2\%$ up to $\lambda \approx 550$ nm. For higher wavelengths, A starts to increase significantly for ITO, peaking at a plasma

wavelength of $\lambda_p \approx 1200$ nm, which is in good agreement with the predicted value (see Figure 1). At the bandgap of the absorber used in this study ($E_G = 1.1$ eV), the parasitic absorption is almost 25%. In the case of ITiO, the plasma wavelength is shifted far into the infrared region ($\lambda_p \approx 2200$ nm), again in good agreement with the calculations (see Figure 1), resulting in only $\approx 5\%$ absorption loss at the absorber band gap.

To estimate the resulting electrical J_{SC} losses at rear illumination, the number of photons absorbed in the TBCs was calculated (A spectra for pristine films), assuming illumination by the AM1.5G spectrum. For simplicity, and to allow for universal conclusions, reflectance losses were ignored and perfect collection as well as complete absorption in the ACIGS were assumed (EQE = 1 for $E > E_{G, \text{ACIGS}}$). Accordingly, the results illustrated at the top in Figure 4 present the maximum possible J_{SC} loss through TBC absorption as a function of the absorber band gap. The corresponding values for the ACIGS used in this study are $J_{SC, \text{loss}} = 4.5$ mA/cm² for ITO and $J_{SC, \text{loss}} = 1.5$ mA/cm² for ITiO. Thus, an up to 3 mA/cm² higher J_{SC} may be expected at rear illumination when ITO is replaced by ITiO as a TBC. The gain in J_{SC} increases even more when the ACIGS bandgap would be reduced to 1.0 eV, which is optimal for bottom cells in a (bifacial) tandem configuration (e.g., with a perovskite-based top cell) [74, 75]. A similar J_{SC} advantage is expected, when ITiO is implemented into a wide-gap ACIGS top cell in a 4-terminal tandem with Si as a bottom cell ($E_{G, \text{Si}} = 1.1$ eV).

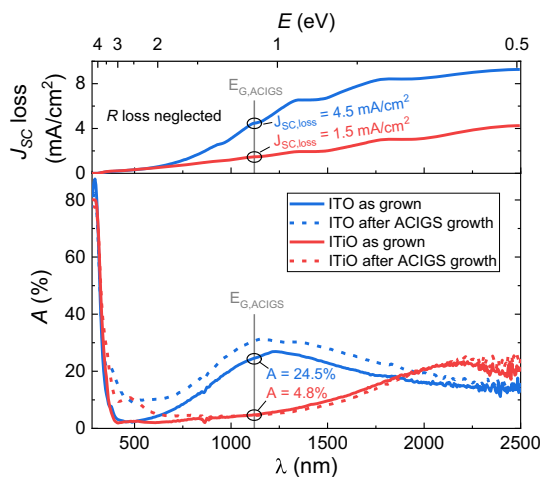


FIGURE 4 | Absorptance spectra of ITO and ITiO before and after absorber deposition, as derived from reflectance and transmission measurements (bottom). In the latter case, the absorber was mechanically removed. This method leads to some ACIGS residuals at the surface, especially for the ITO layer. At the top, the corresponding J_{SC} loss by absorption in the TBC is displayed (same x-axis), assuming rear illumination with the AM1.5G spectrum and neglecting any other electrical or optical losses.

2.3 | Performance of Solar Cells with ITO Versus ITiO Back Contacts

For each sample 16 solar cells were produced. The corresponding solar cell parameters at front illumination, as extracted from current-density versus voltage (JV) measurements, are illustrated as scatter-box plots in Figure 5. The boxes represent the 25%–75% percentiles and the whiskers the minimum and maximum values. One cell per sample was shunted (except for ITO from run 1 that contained two shunted cells), being excluded from the data analysis.

The open circuit voltage (V_{OC}) and FF values vary more for the samples from run number 2. This is due to the very close-stoichiometric absorber composition ($I/III \approx 1.00$), leading to some cells with slightly over-stoichiometric ACIGS. As a result, detrimental secondary phases form, such as Cu_2Se and/or Ag_9GaSe_6 [76], explaining the rather poor performance of some cells from run 2. A KCN etch that could potentially remove those I-rich phases was not applied in the work. However, the very best cells outperform the best ones from the first, off-stoichiometric

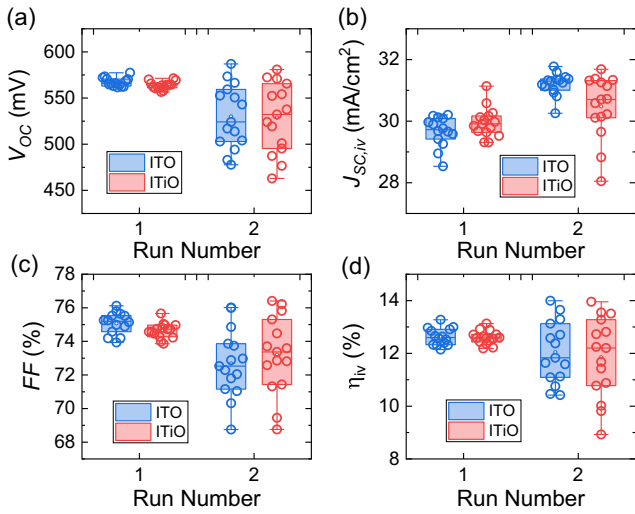


FIGURE 5 | The JV parameters V_{OC} (a), $J_{SC,iv}$ (b), FF (c), and efficiency (d) for all bifacial ACIGS solar cells from this study, using either ITO or ITiO as a transparent back contact. The boxes show the 25%–75% percentiles and the whiskers mark the minimum and maximum values.

run. This is presumably caused by the presence of the I-poor $(Ag,Cu)(In,Ga)_3Se_5$ phase and the generally smaller grain size for the absorber from the first run.

Overall, at front illumination, there is no significant difference between cells with ITO and those with ITiO back contacts. Perhaps most remarkably, both TBCs lead to very high fill factor values $\geq 75\%$ for the best devices, realized by their low sheet resistance in the final device and a sufficiently mitigated GaO_x formation.

The JV characteristics and EQE spectra at front and rear illumination of the best cells from each sample are illustrated in Figure 6. The corresponding solar cell performance parameters are listed in Table 1. To correct for the spectral mismatch between the solar simulator and the AM1.5G spectrum, as well

as for probe shading and slight lateral variations in illumination intensity, the efficiency from JV (η_{iv}) was corrected to $\eta_{qe} = \eta_{iv} \cdot (J_{SC,qe}/J_{SC,iv})$. Here, $J_{SC,qe}$ is the J_{SC} value calculated from integration of the EQE spectra, assuming illumination by the AM1.5G spectrum, and $J_{SC,iv}$ is the value measured in JV analysis.

At front illumination, the highest efficiencies of $\eta_{qe} = 15.4\%$ and 15.1% (without anti-reflection coating) are achieved from the second run for ITO and ITiO TBCs, respectively. Due to the relatively low absorber thickness ($\approx 1 \mu m$), the main loss in J_{SC} arises from incomplete absorption, that is, the optical dominates over the electrical J_{SC} loss. When illuminated from the back, those cells show very comparable V_{OC} values. The fill factor is essentially independent of the illumination side for run number 2, but a smaller FF is measured at rear illumination for the cells from the first run. This may be attributed to the notch-like GGI profile, creating an electrical field that opposes electron collection, or to the smaller grain size, establishing transport barriers for electrons being generated close to the TBC. For all samples, the biggest loss at rear illumination is the significantly reduced J_{SC} . Now, in contrast to front illumination, the main J_{SC} loss can be attributed to recombination in the ACIGS bottom part and possibly at the back interface, signified by a decreasing EQE with decreasing wavelength for $\lambda < 800$ nm and a top EQE level not exceeding ≈ 0.6 for any sample. For the ITO samples, additional losses emanate from the higher FCA and reflection, which will be further analyzed below. Still, the main bottleneck is the too low collection efficiency in the bottom half of the absorber. Improvements may be achieved by an adequate back surface passivation [3, 13, 77, 78], a narrower high-Ga region [2, 11], reduced absorber doping [12–17], and a lower bulk defect density.

Overall, this leads to corresponding top efficiencies of $\eta_{qe} = 8.8\%$ and 10.2% at rear illumination for the cells with ITO and ITiO back contacts, respectively. The higher rear efficiency for the ITiO TBC arises from a 3 mA/cm^2 higher $J_{SC,qe}$ as compared with the cell with ITO (22.7 versus 19.7 mA/cm^2). Spectrally, the J_{SC} gain is reached for $\lambda > 600$ nm, which aligns very well with the higher FCA in this region for ITO as compared with ITiO. However, the higher doping of the ITO does not only lead to a higher FCA, but also to a higher reflectance in the NIR region. Figure 7a,b compares the reflection and absorption losses under rear illumination associated with the respective TBC materials for the cells from run number 2 and presents them alongside the corresponding EQE curves. The total optical loss is approximated as $1 - (1 - R_{cell}) \cdot (1 - A_{TBC})$, with R_{cell} being the reflectance of the cell at rear illumination and A_{TBC} the absorptance of the TBCs (see Figure 4). A significantly higher R_{cell} at $\lambda > 850$ nm is measured for the device with an ITO back contact. The higher NIR reflectivity of the ITO also explains the slightly higher EQE at front illumination in this spectral region for these samples (compare Figure 6).

Overall, the gain in J_{SC} at rear illumination when using ITiO instead of ITO arises to almost equal shares from a reduced FCA and a reduced R_{cell} . To correct for the optical losses from the TBC, the corresponding internal quantum efficiencies (IQE) were derived by normalizing the EQE to the photon flux reaching the absorber at rear illumination ($IQE = EQE / ((1 - R_{cell}) \cdot (1 - A_{TBC}))$). The results are illustrated in Figure 7c. Remaining losses ($IQE \neq 1$) are exclusively originating from recombination or incomplete absorption in the ACIGS film.

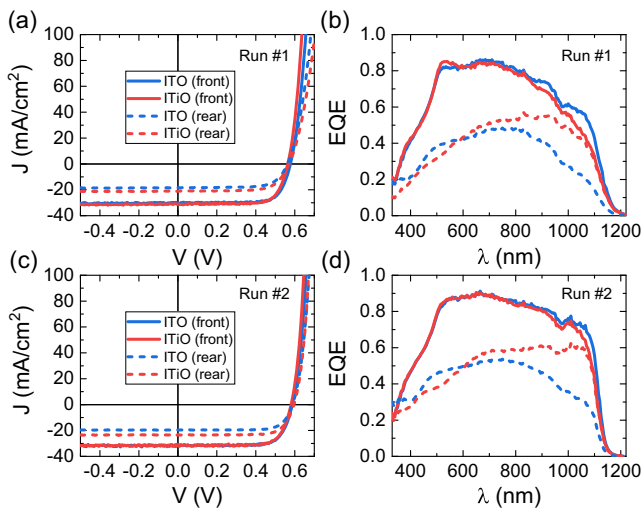


FIGURE 6 | JV characteristics (a,c) and EQE spectra (b,d) at front and rear illumination of the best cells from each ACIGS run, with either ITO or ITiO as a back contact. The deduced solar cell parameters are listed in Table 1.

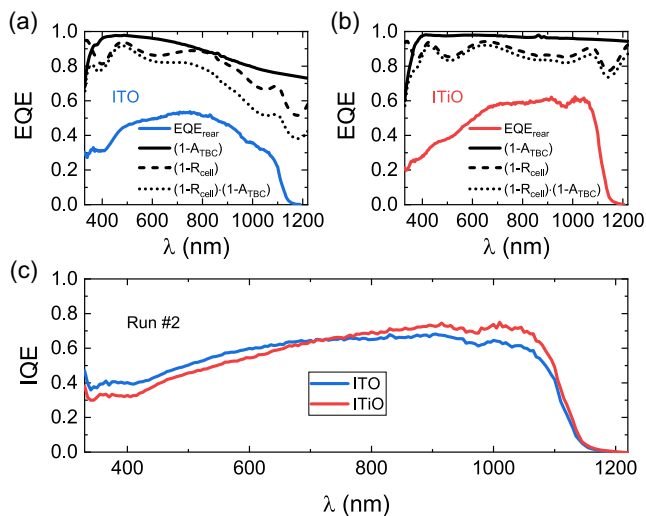


FIGURE 7 | Optical losses at rear illumination through cell reflection (R_{cell}) and FCA in the TBC (A_{TBC}) for the samples with ITO (a) and ITiO (b) back contacts from run number 2. For comparison, the respective EQE spectra are added, too. (c) Corresponding IQE spectra, derived by normalizing the EQE to the photon flux reaching the absorber at rear illumination ($\text{IQE} = \text{EQE}/((1-R_{\text{cell}})(1-A_{\text{TBC}}))$).

The IQE spectra are similar for both TBCs, confirming that the main difference in the cells' J_{SC} can be ascribed to their optical properties. The somewhat higher IQE at short wavelengths for ITO may stem from a slightly wider space charge region as compared to samples with ITiO (282 nm vs. 255 nm in run#2 and 181 nm vs. 145 nm in run#1), as measured from capacity-voltage profiling (not shown here).

In summary, $\text{In}_2\text{O}_3:\text{Ti}$ could be confirmed as a temperature-stable and highly NIR-transparent back contact for ACIGS solar cells and modules. Since the pristine ITiO films were subjected to $T \approx 530^\circ\text{C}$ for 45 min already before absorber deposition, it can be expected that they maintain their exceptional properties also after ACIGS deposition at standard temperatures of $\approx 550^\circ\text{C}$. Future work should focus on improving the collection at rear illumination and thus enhancing the yield of potential bifacial ACIGS modules in the field. Ultimately, to minimize the parasitic FCA in the front electrode (being at least equally detrimental as for the TBC), also the AZO front contact should be replaced by a high-mobility TCO. Here, hydrogenated- In_2O_3 films may be used [51, 79–83], since the front TCO does not have to endure any temperature stress apart from the heating under operation in the field ($<90^\circ\text{C}$). Alternatively, $\text{In}_2\text{O}_3:\text{Me}$ films like ITiO itself can be employed at the front as well, but deposition needs to be done at a temperature $<200^\circ\text{C}$ if CdS is used as a buffer to avoid Cd diffusion into the absorber [84].

3 | Conclusions

Bifacial (Ag,Cu)(In,Ga)Se₂ solar cells with module-compatible (sheet resistance $\leq 10 \Omega/\text{sq}$) $\text{In}_2\text{O}_3:\text{Sn}$ and $\text{In}_2\text{O}_3:\text{Ti}$ back contacts are compared. While both materials exhibit similar and very low resistivities, the $\text{In}_2\text{O}_3:\text{Ti}$ shows significantly reduced free charge carrier absorption in the NIR range, due to the lower doping and high mobility $>100 \text{ cm}^2/\text{Vs}$. Furthermore, both films retain their electrical and optical properties after high-temperature ACIGS

deposition ($T = 450^\circ\text{C}$). As a result, cells with ITiO reach about $3 \text{ mA}/\text{cm}^2$ higher J_{SC} at rear illumination as compared to ITO. The best device achieved a bifaciality factor of 68%, with efficiencies of 15.1% and 10.2% at front and rear illumination, respectively (without anti-reflection coatings). Using ITiO as a transparent back contact in bifacial ACIGS solar cells and modules, almost completely eliminates parasitic absorption losses at rear illumination, leaving recombination at or near the back contact as the remaining loss mechanism. Strategies to further improve the bifaciality factor include a reduced absorber doping, an optimized compositional grading and the passivation of bulk and interface defects.

4 | Experimental Section

4.1 | Solar Cell Processing

The solar cells in this study consist of the following stack: SLG/(ITO or ITiO)/NaF/ACIGS/CdS/ZnO:Al. Both transparent back contacts, ITO and ITiO, were sputter-deposited with thicknesses of 180 nm ($R_{\text{sheet}} \approx 8 \Omega/\text{sq}$) and 240 nm ($R_{\text{sheet}} \approx 10 \Omega/\text{sq}$), respectively. While commercial ITO (*Xop Glass*, $\text{In}_2\text{O}_3:\text{SnO}_2 = 90:10 \text{ wt.}\%$ target) was used, the ITiO films were processed in-house, using an Orion 8 sputtering system (AJA International). Films were grown using RF sputtering (target composition of $\text{In}_2\text{O}_3:\text{TiO}_2 = 99:1 \text{ wt.}\%$), at a power density of $3.94 \text{ W}/\text{cm}^2$, at a pressure of 1 mTorr in an Ar atmosphere, at 500°C substrate temperature for 30 min. This was then followed by a 45-min postdeposition anneal at 530°C under high vacuum. The TBC films were coated with a 5 nm-thick NaF precursor layer, to allow for sufficient Na incorporation into the absorber.

A three-stage (group I-poor \rightarrow group I-rich \rightarrow group I-poor) co-evaporation process was applied to grow the ACIGS films at a maximum temperature of 450°C . To implement a bandgap grading toward the back contact, higher Ga and lower In evaporation rates were chosen in the initial growth stages. Further details can be found in [70]. A heavy alkali postdeposition treatment was not implemented. All solar cells in this study originate from two ACIGS deposition runs, leading to an ACIGS thickness of $1 \mu\text{m}$ with similar GGI ≈ 0.2 and AAC ≈ 0.1 . The first run produced off-stoichiometric (I/III ≈ 0.8) and the second run close-stoichiometric (I/III ≈ 1.0) ACIGS films. Both runs contained samples with ITO and ITiO back contacts.

After absorber deposition (<15 -min air exposure), a 55 nm thick CdS buffer layer was grown via chemical bath deposition at 60°C . Finally, a double-layer of ZnO:Al was sputtered on top. A 30 nm-thick, highly resistive AZO film ($R_{\text{sheet}} > 1 \text{ k}\Omega/\text{sq}$, using high oxygen flow) was followed by a 180 nm-thick conductive AZO layer ($R_{\text{sheet}} \approx 40 \Omega/\text{sq}$). The completed samples were sectioned into 16 individual solar cells (area = 0.1 cm^2) via local, selective removal of the buffer and window layers (etching in HCl), allowed by a photolithography masking process (see, e.g., supporting information in [14, 44]).

4.2 | Material Characterization

The integral absorber compositions were measured with a Panalytical Epsilon 5 XRF spectrometer, using a reference ACIGS

sample with known composition. Elemental depth profiles were deduced from GDOES in a Spectrum Analytik GDA 750HR system (quantification by cross-calibration to XRF compositions). Reflectance and transmission measurements of the TBC films were conducted in the spectral range of $\lambda = 280\text{--}2500\text{ nm}$ in a Perkin Elmer Lambda 900 spectrometer with an integrating sphere. The absorbance was then calculated via $A = 1 - T - R$. A Zeiss Merlin SEM was used to investigate the solar cell cross sections. The sheet resistance of the front TCO was measured in a linear 4-point probe configuration. For the Hall-effect measurements, each sample was cut into a $1\text{ cm} \times 1\text{ cm}$ piece from its center, and metal alloy contacts were applied to the corners using an ultrasonic soldering iron. The measurements were conducted in the dark using an Ecopia HMS-3000 system in the van-der-Pauw configuration to determine conductivity, carrier concentration, and mobility. A drive current was applied to the sample under a perpendicular magnetic field of $\approx 0.55\text{ T}$. The resulting Hall voltage indicates the dominant carrier type based on its polarity. Carrier concentration was first calculated from the Hall voltage together with the applied drive current, the magnetic field strength, and the sample thickness. The carrier mobility was then determined from the measured conductivity and the calculated carrier concentration.

4.3 | Electro-Optical Characterization of Solar Cells

The JV (all 16 cells per sample) and EQE (only best cell for each sample) measurements of completed solar cells were done using home-built setups. To avoid any reflection from the stage surfaces, a highly absorbing, black sponge was placed underneath the solar cells. The JV characteristics were measured in forward voltage sweep at a temperature of $\approx 25^\circ\text{C}$ under illumination by a class AAA solar simulator from G2V (Pico), using light emitting diode arrays. The light intensity was adjusted to match the J_{SC} value at 1 sun irradiance of a calibrated Si reference solar cell. After measuring JV on all solar cells, the EQE was measured only on the best cells for each sample. Subsequently, the JV characteristics of the best cells were measured at rear illumination (same light intensity as for front illumination). Since the sample contacting was done at the non-illuminated side, active cooling was not possible at rear illumination. Thus, illumination was kept as short as possible and a sample temperature of $\approx 22^\circ\text{C}$ (i.e. ambient temperature) can be assumed. Capacitance-voltage profiling was conducted from $V = +0.4\text{ V}$ to -0.6 V at 60 kHz and an amplitude of 25 mV , using an Agilent 4284 A precision LCR meter and a Keithley 2401 source meter. A dielectric constant of $\epsilon_r = 10$ was assumed for the ACIGS material in this study.

Acknowledgments

This work was financially supported by the European union programme HORIZON (project number 101122203, HORIZON-CL5-2022-D3-03 (Hi-BITS)) as well as the EPSRC (UK) (EP/V013858/1).

Conflicts of Interest

The authors declare no conflicts of interest.

Data Availability Statement

The data that support the findings of this study are available from the corresponding author upon reasonable request.

References

1. J. Keller, K. Kiselman, O. Donzel-Gargand, et al., "High-Concentration Silver Alloying and Steep Back-Contact Gallium Grading Enabling Copper Indium Gallium Selenide Solar Cell with 23.6% Efficiency," *Nature Energy* 9 (2024): 46.
2. S. C. Yang, T. Y. Lin, M. Ochoa, et al., "Efficiency Boost of Bifacial Cu(In,Ga)Se₂ Thin-Film Solar Cells for Flexible and Tandem Applications with Silver-Assisted Low-Temperature Process," *Nature Energy* 8 (2023): 40.
3. J. Keller, W.-C. Chen, L. Riekehr, T. Kubart, T. Törndahl, and M. Edoff, "Bifacial Cu(In,Ga)Se₂ Solar Cells Using Hydrogen-Doped In₂O₃ Films as a Transparent Back Contact," *Progress in Photovoltaics: Research and Applications* 26 (2018): 846.
4. J. Keller, N. S. Nilsson, A. Aijaz, et al., "Using Hydrogen-Doped In₂O₃ Films as a Transparent Back Contact in (Ag,Cu)(In,Ga)Se₂ Solar Cells," *Progress in Photovoltaics: Research and Applications* 26 (2018): 159.
5. C. Spindler, F. Babbe, M. H. Wolter, et al., "Electronic Defects in Cu(In,Ga)Se₂: Towards a Comprehensive Model," *Physical Review Materials* 3 (2019): 090302.
6. J. Pohl and K. Albe, "Intrinsic Point Defects in CuInSe₂ and CuGaSe₂ as Seen via Screened-Exchange Hybrid Density Functional Theory," *Physical Review B* 87 (2013): 245203.
7. S. Hegedus and W. N. Shafarman, "Thin-Film Solar Cells: Device Measurements and Analysis," *Progress in Photovoltaics: Research and Applications*, 12 (2004): 155.
8. B. Huang, S. Chen, H. Deng, et al., "Origin of Reduced Efficiency in Cu(In,Ga)Se₂ Solar Cells With High Ga Concentration: Alloy Solubility Versus Intrinsic Defects," *IEEE Journal of Photovoltaics* 4 (2014): 477.
9. M. R. Balboul, H. W. Schock, S. A. Fayak, A. A. El-Aal, J. H. Werner, and A. A. Ramadan, "Correlation of Structure Parameters of Absorber Layer with efficiency of Cu(In,Ga)Se₂ Solar Cell," *Applied Physics A* 92 (2008): 557.
10. M. Raghuvanshi, E. Cadel, P. Pareige, et al., "Influence of Grain Boundary Modification on Limited Performance of Wide Bandgap Cu(In,Ga)Se₂ Solar Cells," *Applied Physics Letters* 105 (2014): 013902.
11. A. Ali, D. H. Jeon, W. Kim, et al., "Highly Efficient Bifacial Narrow Bandgap Ag-CuInSe₂ Solar Cells on ITO," *Advanced Energy Materials* 15 (2025): 2500899.
12. P. Pearson, J. Keller, L. Stolt, and C. P. Björkman, "Investigating the Role of Ag and Ga Content in the Stability of Wide-Gap (Ag,Cu)(In,Ga)Se₂ Thin-Film Solar Cells," *Physica Status Solidi (B)* 260 (2023): 2300170.
13. J. Keller, S. Mudgal, C. Häggglund, K. Kiselman, and M. Edoff, "Ultrathin AlO_x Films for Back Contact Passivation in Bifacial Wide-Gap (Ag,Cu)(In,Ga)Se₂ Solar Cells," *Solar RRL* 9 (2025): 2500101.
14. J. Keller, L. Stolt, O. Donzel-Gargand, A. F. Violas, T. Kubart, and M. Edoff, "Bifacial Wide-Gap (Ag,Cu)(In,Ga)Se₂ Solar Cell with 13.6% Efficiency Using In₂O₃:W as a Back Contact Material," *Solar RRL* 8 (2024): 2400430.
15. A. Kanevce, S. Essig, S. Paetel, W. Hempel, D. Hariskos, and T. M. Friedlmeier, "Impact of Ag Content on Device Properties of Cu(In,Ga)Se₂ Solar Cells," *EPJ Photovoltaics* 13 (2022): 1.
16. N. Valdes, J. W. Lee, and W. Shafarman, "Comparison of Ag and Ga Alloying in Low Bandgap CuInSe₂-Based Solar Cells," *Solar Energy Materials and Solar Cells* 195 (2019): 155.
17. P. T. Erslev, J. Lee, G. M. Hanket, W. N. Shafarman, and J. D. Cohen, "The Electronic Structure of Cu(In_{1-x}Ga_x)Se₂ Alloyed with Silver," *Thin Solid Films* 519 (2011): 7296.

18. M. J. Shin, S. Park, A. Lee, et al., "Bifacial Photovoltaic Performance of Semitransparent Ultrathin Cu(In,Ga)Se₂ Solar Cells with Front and Rear Transparent Conducting Oxide Contacts," *Applied Surface Science* 535 (2021): 147732.
19. T. Nakada, Y. Hirabayashi, T. Tokado, D. Ohmori, and T. Mise, "Novel Device Structure for Cu(In,Ga)Se₂ Thin Film Solar Cells Using Transparent Conducting Oxide Back and Front Contacts," *Solar Energy* 77 (2004): 739.
20. R. Caballero, S. Siebentritt, K. Sakurai, C. A. Kaufmann, and M. C. Lux-Steiner, in *2006 IEEE 4th World Conference on Photovoltaic Energy Conference*, Waikoloa, HI, 2006, 479–482, <https://doi.org/10.1109/WCPEC.2006.279495>.
21. W. Ohm, W. Riedel, U. Aksünger, et al., *2015 IEEE 42nd Photovoltaic Specialist Conference (PVSC)*, New Orleans, LA, 2015, 1–5, <https://doi.org/10.1109/PVSC.2015.7356416>.
22. F. Mollica, M. Jubault, F. Donsanti, et al., "Light Absorption Enhancement in Ultra-Thin Cu(In,Ga)Se₂ Solar Cells by Substituting the Back-Contact with a Transparent Conducting Oxide Based Reflector," *Thin Solid Films* 633 (2017): 202.
23. M. Mazzer, S. Rampino, G. Spaggiari, et al., "Bifacial CIGS Solar Cells Grown by Low Temperature Pulsed Electron Deposition," *Solar Energy Materials and Solar Cells* 166 (2017): 247.
24. M. J. Shin, J. H. Jo, A. Cho, et al., "Semi-Transparent Photovoltaics Using Ultra-Thin Cu(In,Ga)Se₂ Absorber Layers Prepared by Single-Stage Co-Evaporation," *Solar Energy* 181 (2019): 276.
25. M. J. Shin, A. Lee, A. Cho, et al., "Semitransparent and Bifacial Ultrathin Cu(In,Ga)Se₂ Solar Cells via a Single-Stage Process and Light-Management Strategy," *Nano Energy* 82 (2021): 105729.
26. N. Cavallari, F. Pattini, S. Rampino, et al., "Low Temperature Deposition of Bifacial CIGS Solar Cells on Al-Doped Zinc Oxide Back Contacts," *Applied Surface Science* 412 (2017): 52.
27. N. Hamada, T. Nishimura, J. Chantana, Y. Kawano, T. Masuda, and T. Minemoto, "Fabrication of Flexible and Bifacial Cu(In,Ga)Se₂ Solar Cell with Superstrate-Type Structure Using a Lift-Off Process," *Solar Energy* 199 (2020): 819–825.
28. J. Chantana, H. Arai, and T. Minemoto, "Trap-Assisted Recombination for Ohmic-Like Contact at p-Type Cu(In,Ga)Se₂/Back n-Type TCO Interface in Superstrate-Type Solar Cell," *Journal of Applied Physics* 120 (2016): 045302.
29. T. Schneider and R. Scheer, *36th European PV Solar Energy Conference and Exhibition* Marseille, France, 2019, 684.
30. T. Schneider, T. Hölscher, H. Kempa, and R. Scheer, *37th European Photovoltaic Solar Energy Conference and Exhibition*, 2020, 621.
31. Y. S. Son, H. Yu, J. K. Park, et al., "Control of Structural and Electrical Properties of Indium Tin Oxide (ITO)/Cu(In,Ga)Se₂ Interface for Transparent Back-Contact Applications," *The Journal of Physical Chemistry C* 123 (2019): 1635.
32. M. Saifullah, D. Kim, J. S. Cho, et al., "The Role of NaF Post-Deposition Treatment on the Photovoltaic Characteristics of Semitransparent Ultrathin Cu(In,Ga)Se₂ Solar Cells Prepared on Indium-Tin-Oxide Back Contacts: A Comparative Study," *Journal of Materials Chemistry A* 7 (2019): 21843.
33. A. Jeong, J. M. Choi, H.-J. Lee, et al., "Transparent Back-Junction Control in Cu(In,Ga)Se₂ Absorber for High-Efficiency, Color-Neutral, and Semitransparent Solar Module," *Progress in Photovoltaics: Research and Applications* 30(2022): 713.
34. Y. Li, G. Yin, Y. Gao, T. Köhler, J. Lucassen, and M. Schmid, "Sodium Control in Ultrathin Cu(In,Ga)Se₂ Solar Cells on Transparent Back Contact for Efficiencies Beyond 12%," *Solar Energy Materials and Solar Cells* 223 (2021): 110969.
35. Y. Li, G. Yin, and M. Schmid, "Bifacial Semi-Transparent Ultra-Thin Cu(In,Ga)Se₂ Solar Cells on ITO Substrate: How ITO Thickness and Na Doping Influence the Performance," *Solar Energy Materials and Solar Cells* 234 (2022): 111431.
36. T. Schneider, C. Dethloff, T. Hölscher, H. Kempa, and R. Scheer, "Comparison of Mo and ITO Back Contacts in CIGSe Solar Cells: Vanishing of the Main Capacitance Step," *Progress in Photovoltaics: Research and Applications* 30 (2022): 191.
37. A. Mavlonov, J. Chantana, T. Nishimura, et al., "Superstrate-Type Flexible and Bifacial Cu(In,Ga)Se₂ Thin-Film Solar Cells with In₂O₃:SnO₂ Back Contact," *Solar Energy* 211 (2020): 725.
38. A. Mavlonov, T. Nishimura, J. Chantana, Y. Kawano, and T. Minemoto, "Effect of an Ohmic Back Contact on the Stability of Cu(In,Ga)Se₂-Based Flexible Bifacial Solar Cells," *Applied Physics Letters* 119 (2021): 103903.
39. J. H. Choi, K. Kim, Y. J. Eo, et al., "Wide-Bandgap CuGaSe₂ Thin Film Solar Cell Fabrication Using ITO Back Contacts," *Vacuum* 120 (2015): 42.
40. D. Abou-Ras, G. Kostorz, D. Bremaud, et al., "Formation and Characterisation of MoSe₂ for Cu(In,Ga)Se₂ Based Solar Cells," *Thin Solid Films* 480-481 (2005): 433.
41. D. Kim, S. S. Shin, Y. Jo, et al., "Practical Enhancements in Current Density and Power Generation of Bifacial Semitransparent Ultrathin CIGSe Solar Cells via Utilization of Wide Bandgap Zn-Based Buffer," *Advanced Science* 9 (2022): 2105436.
42. C. Rath, Y. Gao, T. Köhler, and M. Schmid, "Impact of Band-gap Gradient in Semi-Transparent and Bifacial Ultra-Thin Cu(In,Ga)Se₂ Solar Cells," *Advanced Materials Interfaces* 11 (2024): 2400085.
43. M. J. Shin, A. Lee, J. H. Park, et al., "Ultrathin Cu(In,Ga)Se₂ Transparent Photovoltaics: an Alternative to Conventional Solar Energy-Harvesting Windows," *Nano Energy* 92 (2022): 106711.
44. J. Keller, L. Stolt, O. Donzel-Gargand, T. Kubart, and M. Edoff, "Wide-Gap Chalcopyrite Solar Cells with Indium Oxide-Based Transparent Back Contacts," *Solar RRL* 6 (2022): 2200401.
45. J. Keller, S. Mudgal, N. M. Martin, O. Donzel-Gargand, and M. Edoff, "Rubidium Fluoride Absorber Treatment for Wide-Gap and Bifacial Ag(In,Ga)Se₂ Solar Cells," *Solar RRL* 9 (2025): 2500423.
46. R. Gutzler, C. Y. Song, D. Hariskos, et al., "Assessment of Transparent Conductive Oxides as Back Contacts for Inline-Fabricated Cu(In,Ga)Se₂ Solar Cells," *Journal of Physics: Energy* 7 (2025): 045018.
47. T. Nakada, T. Miyano, R. Hashimoto, Y. Kanda, and T. Mise, *22nd European Photovoltaic Solar Energy Conference*, 3–7 September 2007 Milan, Italy, pp. 1870.
48. T. J. Coutts, D. L. Young, and X. Li, "Characterization of Transparent Conducting Oxides," *MRS Bulletin* 25 (2000): 58.
49. T. Koida, J. Nishinaga, H. Higuchi, et al., "Comparison of ZnO:B and ZnO:Al Layers for Cu(In,Ga)Se₂ Submodules," *Thin Solid Films* 614 (2016): 79.
50. J. N. Duenow, D. M. Wood, B. Egaas, T. A. Gessert, R. Noufi, and T. J. Coutts, *33rd IEEE Photovoltaic Specialists Conference*, San Diego, 2008.
51. J. Keller, A. Aijaz, F. Gustavsson, et al., "Direct Comparison of Atomic Layer Deposition and Sputtering of In₂O₃:H Used as Transparent Conductive Oxide Layer in CuIn_{1-x}Ga_xSe₂ Thin Film Solar Cells," *Solar Energy Materials and Solar Cells* 157 (2016): 757.
52. T. Koida, Y. Ueno, and H. Shibata, "In₂O₃-Based Transparent Conducting Oxide Films with High Electron Mobility Fabricated at Low Process Temperatures," *Physica Status Solidi (A)* 215 (2018): 1700506.
53. J. E. N. Swallow, B. A. D. Williamson, T. J. Whittles, et al., "Self-Compensation in Transparent Conducting F-Doped SnO₂," *Advanced Functional Materials* 28 (2018): 1701900.
54. S. Calnan and A. N. Tiwari, "High Mobility Transparent Conducting Oxides for Thin Film Solar Cells," *Thin Solid Films* 518 (2010): 1839.

55. M. W. Rowell and M. D. McGehee, "Transparent Electrode Requirements for Thin Film Solar Cell Modules," *Energy & Environmental Science* 4 (2011): 131.
56. D. A. Jacobs, K. R. Catchpole, F. J. Beck, and T. P. White, "A Re-Evaluation of Transparent Conductor Requirements for Thin-Film Solar Cells," *Journal of Materials Chemistry A* 4 (2016): 4490.
57. N. Preissler, O. Bierwagen, A. T. Ramu, and J. S. Speck, "Electrical Transport, Electrothermal Transport, and Effective Electron Mass in Single-Crystalline In_2O_3 Films," *Physical Review B* 88 (2013): 085305.
58. T. C. Rödel, J. Dai, F. Fortuna, et al., "High-Density Two-Dimensional Electron System Induced by Oxygen Vacancies in ZnO ," *Physical Review Materials* 2 (2018): 051601.
59. J. S. Kim, J. H. Jeong, J. K. Park, et al., "Optical Analysis of Doped ZnO Thin Films Using Nonparabolic Conduction-Band Parameters," *Journal of Applied Physics* 111 (2012): 123507.
60. G. Rey, C. TERNON, M. Modreanu, X. Mescot, V. Consonni, and D. Bellet, "Electron Scattering Mechanisms in Fluorine-Doped SnO_2 Thin Films," *Journal of Applied Physics* 114 (2013): 183713.
61. T. Koida, H. Fujiwara, and M. Kondo, "Hydrogen-Doped In_2O_3 as High-Mobility Transparent Conductive Oxide," *Japanese Journal of Applied Physics* 46 (2007): 685.
62. T. Koida and Y. Ueno, "Thermal and Damp Heat Stability of High-Mobility In_2O_3 -Based Transparent Conducting Films Fabricated at Low Process Temperatures," *Physica Status Solidi (A)* 218 (2021): 2000487.
63. J. Nomoto, T. Koida, I. Yamaguchi, and T. Nakajima, "Key Sputtering Parameters for Precursor In_2O_3 Films to Achieve High Carrier Mobility," *ACS Applied Materials & Interfaces* 16 (2024): 64113.
64. Y. Abe and N. Ishiyama, "Titanium-Doped Indium Oxide Films Prepared by d.c. Magnetron Sputtering Using Ceramic Target," *Journal of Materials Science* 41 (2006): 7580.
65. M. F. A. M. Van Hest, M. S. Dabney, J. D. Perkins, D. S. Ginley, and M. P. Taylor, "Titanium-Doped Indium Oxide: A High-Mobility Transparent Conductor," *Applied Physics Letters* 87 (2005): 032111.
66. S. C. Yang, J. Sastre, M. Krause, et al., "Silver-Promoted High-Performance $(\text{Ag,Cu})(\text{In,Ga})\text{Se}_2$ Thin-Film Solar Cells Grown at Very Low Temperature," *Solar RRL* 5 (2021): 2100108.
67. G. M. Hanket, J. H. Boyle, and W. N. Shafarman, *34th IEEE Photovoltaic Specialists Conference*, Philadelphia, PA, 2009, 001240.
68. G. Kim, W. M. Kim, J. K. Park, D. Kim, H. Yu, and J. H. Jeong, "Thin Ag Precursor Layer-Assisted Co-Evaporation Process for Low-Temperature Growth of $\text{Cu}(\text{In,Ga})\text{Se}_2$ Thin Film," *ACS Applied Materials & Interfaces* 11 (2019): 31923.
69. J. Keller, R. Schlesiger, I. Riedel, et al., "Grain Boundary Investigations on Sulfurized $\text{Cu}(\text{In,Ga})(\text{S,Se})_2$ Solar Cells Using Atom Probe Tomography," *Solar Energy Materials and Solar Cells* 117 (2013): 592.
70. E. Yakovleva, A. F. Violas, O. Donzel-Gargand, et al., *IEEE 53rd Photovoltaic Specialists Conference (PVSC)*, Montreal, QC, Canada, 2025, 0229.
71. K. V. Sopiha, J. K. Larsen, O. Donzel-Gargand, et al., "Thermodynamic Stability, Phase Separation and Ag Grading in $(\text{Ag,Cu})(\text{In,Ga})\text{Se}_2$ Solar Absorbers," *Journal of Materials Chemistry A* 8 (2020): 8740.
72. E. Cadel, N. Barreau, J. Kessler, and P. Pareige, "Atom Probe Study of Sodium Distribution in Polycrystalline $\text{Cu}(\text{In,Ga})\text{Se}_2$ Thin Film," *Acta Materialia* 58 (2010): 2634.
73. O. Cojocaru-Mirédin, P. Choi, D. Abou-Ras, S. S. Schmidt, R. Caballero, and D. Raabe, "Characterization of Grain Boundaries in $\text{Cu}(\text{In,Ga})\text{Se}_2$ Films Using Atom-Probe Tomography," *IEEE Journal of Photovoltaics* 1 (2011): 207.
74. A. S. Brown and M. A. Green, "Detailed Balance Limit for the Series Constrained Two Terminal Tandem Solar Cell," *Physica E: Low-Dimensional Systems & Nanostructures* 14 (2002): 96.
75. R. K. Kothandaraman, Y. Jiang, T. Feurer, A. N. Tiwari, and F. Fu, "Near-Infrared-Transparent Perovskite Solar Cells and Perovskite-Based Tandem Photovoltaics," *Small Methods* 4 (2020): 2000395.
76. J. C. Mikkelsen, " $\text{Ag}_2\text{Se}_2\text{Ga}_2\text{Se}_3$ Pseudobinary Phase Diagram," *Materials Research Bulletin* 12 (1977): 497.
77. W. Ohm, W. Riedel, U. Aksünger, et al., *IEEE 42nd Photovoltaic Specialist Conference (PVSC)*, New Orleans, LA, 2015, 1.
78. F. Mollica, (*PhD Thesis, Université Pierre et Marie Curie - Paris VI*, 2016).
79. T. Koida, Y. Ueno, J. Nishinaga, et al., " $\text{Cu}(\text{In,Ga})\text{Se}_2$ Solar Cells with Amorphous In_2O_3 -Based Front Contact Layers," *ACS Applied Materials & Interfaces* 9 (2017): 29677.
80. J. Keller, J. Lindahl, M. Edoff, L. Stolt, and T. Törndahl, "Potential Gain in Photocurrent Generation for $\text{Cu}(\text{In,Ga})\text{Se}_2$ Solar Cells by Using In_2O_3 as a Transparent Conductive Oxide Layer," *Progress in Photovoltaics: Research and Applications* 24 (2016): 102.
81. J. Keller, L. Stolt, M. Edoff, and T. Törndahl, "Atomic Layer Deposition of In_2O_3 Transparent Conductive Oxide Layers for Application in $\text{Cu}(\text{In,Ga})\text{Se}_2$ Solar Cells with Different Buffer Layers," *Physica Status Solidi (A)* 213 (2016): 1541.
82. D. A. Garzon, M. Alves, P. Sousa, et al., "Comparative Study of Cd-Free $\text{Cu}(\text{In,Ga})\text{Se}_2$ Solar Cells with Amorphous $\text{In}_2\text{O}_3\text{:H}$ and ZnO:Al Front Contact Layers," *Journal of Physics: Energy* 7 (2025): 035011.
83. T. Jäger, Y. E. Romanyuk, S. Nishiwaki, et al., "Hydrogenated Indium Oxide Window Layers for High-Efficiency $\text{Cu}(\text{In,Ga})\text{Se}_2$ Solar Cells," *Journal of Applied Physics* 117 (2015): 205301.
84. A. Koprek, O. Cojocaru-Mirédin, R. Wuerz, C. Freysoldt, B. Gault, and D. Raabe, "Cd and Impurity Redistribution at the CdS/CIGS Interface After Annealing of CIGS-Based Solar Cells Resolved by Atom Probe Tomography," *IEEE Journal of Photovoltaics* 7 (2017): 313.